

The 3D Geometry of Dark Matter Halos

J.-F. Bequaert and F. Combes

DEMIRM, Observatoire de Paris, 61 Av. de l'Observatoire, F-75014, Paris, France

May 13, 2019

Abstract. The thickness of the neutral hydrogen layer, coupled with the rotation curve, traces the outer dark matter potential. We estimate the amplitude of the flaring in spiral galaxies from a 3D model of the HI gas. Warps in particular are explicitly parametrized in the form of an harmonical density wave. Applying our method to the galaxy NGC 891, the only model that could fit the observations, and in particular the HI at large height above the plane, includes a strong warp with a line of node almost coinciding with the line of sight. This high-Z HI is not observed at the most extreme velocity channels, those corresponding to high rotational velocities. This is accounted for by the model, since orbits in the tilted planes are not circular, but elongated, with their minor axis in the galaxy plane. Their velocity on the major axis (i.e. at their maximal height above the plane) is then 30% less than in the plane. We finally connect the modelled vertical outer gaseous distribution to the dark matter through hydrodynamical and gravitational equations. Under the assumption of isotropy of the gaseous velocity dispersion, we conclude on a very flattened halo geometry for the galaxy NGC 891 ($q \approx 0.2$), while a vertical velocity dispersion smaller than the radial one would lead to a less flattened Dark Matter Halo ($q \approx 0.4 - 0.5$). Both results however suggests that dark matter is dissipative or has been strongly influenced by the gas dynamics.

Key words: Galaxies: general – Galaxies: halos – Galaxies: individual: NGC891 – Galaxies: ISM – Galaxies: kinematics and dynamics – Cosmology: dark matter

1. Introduction

Knowing the 3D shape and extent of the Dark Matter Halos embedding galaxies (hereafter DMHs) is of particular importance: it can constrain the nature of the dark matter itself, and in particular its dissipative character. Even in the frame of a given dark matter model, such as CDM, the shape of DMHs can constrain the galaxy formation scenarios, including gas infall (e.g. Dubinski &

Carlberg 1991, Dubinski 1994). Little is known about the shape of DMHs, and in particular their flattening and extent. Most of the best evidence of the existence of DMHs has been gained through HI rotation curves (see the review by Freeman 1993), and are limited to the HI disk. The dynamics of satellites (Zaritsky & White 1994) can extend further but with strong biases. Techniques based on gravitational lensing, virial masses or X-rays can reach constraints at much larger scales. In a recent paper, David et al (1995) observed a decrease of the mass-to-light ratio [M_{tot}/M_{lum}] between galaxies and clusters, suggesting that the dark matter in the universe is essentially confined around individual galaxies.

Since the best tool to test DMHs, HI rotation curves, only provide azimuthal constraints, we have to find a vertical signature of these halos on the plane of spiral galaxies (for which we have the most accurate rotation curves). The knowledge of both the HI velocity dispersion and plane thickness is a mean to test the shape of DMHs. Since it has been measured in face-on galaxies a constant HI velocity dispersion with radius (e.g. Dickey et al 1990), the idea is to use the flaring of the neutral hydrogen (i.e. radial increase of the thickness of the HI layer towards external parts), as a vertical tracer of the dark matter potential. The HI layer in an isolated exponential stellar disk is expected to flare exponentially with radius; but the amplitude of the flaring is expected to be modified with the presence of surrounding dark mass, depending on its geometry. The first serious attempt using the flaring of the gas layers has been done by R. Olling (1995) who concluded on a very pronounced flattening of the halo of NGC 4244 of $(\frac{z}{a} =)q = 0.2_{-0.1}^{+0.3}$ (i.e. E5-E9), the large error being mostly due to the uncertainties on the velocity dispersion of the gas. Other techniques exist: the first one is to constrain the flattening using Polar Rings (i.e. two “orthogonal” rotation curves). Sackett and Sparke (1990) found using this way a constraint on NGC4650a 's DMH of E6-E7, while more recently the same study placed a E5 constraint on A0136-0801's DMH (Sackett and Pogge, 1995). However, the method using Polar Rings is intrinsically uncertain, and the Polar Ring itself can totally change the DMH geometry, as shown by Combes & Arnaboldi (1995). A

related method consists in using the dynamics of a precessing dusty disk: Steiman-Cameron et al (1992) inferred this way for the SO galaxy NGC4753 a quasi-spherical E1 DMH. Deriving the DMH geometry by the flaring law has however the advantage to be applicable to a larger sample of galaxies : every spiral galaxy with an inclination $\geq 60^\circ$ can be an acceptable candidate (Olling 1995).

The large range of values found until now for DMH flattenings (from E1 to E9) can be interpreted either in the way that the local universe is very heterogeneous, or, and this is more probable, that methods quoted above are dominated by errors and uncertainties.

Determining the flaring of the gas in disk galaxies is a difficult task, due to projection uncertainties (galaxies are never perfectly edge-on) and due to the presence of warps, that deform the gas plane and thus modifies our perception of its vertical distribution. We remark that in the literature concerning the determination of the flaring of the gas in spiral galaxies, warps are never taken into account, so that the validity of the flaring curves obtained remains correct only for the inner unwarped disk, precisely where the dark matter halo is undetectable: a statistical analysis of the morphology of 167 rotation curves of spiral galaxies indeed shows that the dynamics inside the optical regions is not usually controlled by the dark component (Corradi & Capaccioli, 1990, and Freeman, 1993). A predictive and consistent theory of warps still does not exist (Binney, 1992) even if we may have new hints about it (Masset & Tagger, 1996). We still do not have a general model of warps, an equation connecting the shape of the warp to the fundamental parameters of the galaxy, so that most of the time, the warp is ignored in models. The flaring curves given in the literature are therefore overestimated (nearly all galaxies being more or less warped). The DMH flattening is consequently generally underestimated (see figure 10 of Olling’s Thesis, 1995 and our Fig 15): halos are certainly even more “disk-like” if we model and subtract a warp. More generally and as far as we know, no attempt has been made to search different “geometries” than ellipsoidal. Combes and Arnaboldi (1995) suggested that dark matter could be ring-like, in the same category of geometry than the Pfenniger & Combes (1994) model of dark matter which is a disk. A question arises finally: can we use “warps” as a supplement vertical signature ? The idea that one may take the shape of warps as another constraint on the DMH geometry (Sparke & Casertano 1988) is more and more controversial. Tubbs & Sanders (1979) and Sparke & Casertano (1988) developed the idea that the shape of warps can help to constrain the DMH geometry. But this is extremely model-dependent. A spherical potential can maintain a warp forever (Tubbs & Sanders, 1979) while a self-gravitating warp also solves the problem of differential precession (Sparke & Casertano 1988, Pfenniger et al 1994). The HI thickness might thus be the more reliable vertical signature of the halo on the outer disk.

2. Modeling the 3D distribution of the HI gas in spiral galaxies

In this paper we develop a theoretical method to derive constraints on the DMH flattening from the observed HI thickness and we apply it to the nearby galaxy NGC 891, which is almost edge-on, and on which an abundant literature exists. The HI data of this galaxy used here are from Rupen (1991). NGC 891 is classified as an Sb galaxy, member of the NGC 1023 group, at a distance of 10.0 Mpc (Rupen 1991, for $H_0 = 75 \text{ km/s/Mpc}$) and of systemic velocity 535 km/s. This galaxy is not obviously warped, and it has a gaseous large-scale asymmetry (southern extension up to $R_{HI,south} = 26.5 \text{ kpc}$), while in the north the gas stops surprisingly much before the optical radius ($R_{HI,north} = 18.375 \text{ kpc}$ while $R_{opt} = 22.3 \text{ kpc}$). Our subject of interest is to determine if there is indeed a warp, then estimate the true HI thickness and amplitude of the flaring. The entire modeling is geometrical and kinematical, so that the question of assuming any time-dependency of warps or the spiral arms do not raise here. We give ourselves a 3D HI model and adapt the parameters to the observations, we do not simulate an evolution of the system as does the N-Body technique.

2.1. Modeling the HI infinitely thin disk from the integrated flux along the line of sight

The gaseous surface density can be represented by the real part of the Fourier development:

$$\Sigma_g(R, \Theta) = A_0(R) + \sum_{i=1}^{\infty} A_m(R) e^{i(k_m R - m(\Theta - \Theta_m))}$$

For quasi edge-on galaxies, because of the projection, the Θ information vanishes, and spiral arms, in the best case, can be rebuilt with spectral cube modeling (section 4), but not found with the technique used here. The technique is to consider the zero moment map of a nearly edge-on galaxy (i.e. the integrated HI flux). The r.m.s. noise in the channel maps of NGC 891, associated with the synthesized beam of $FWHM = 20'' \times 20''$, is 0.780 mJy/beam. The velocity resolution, after Hanning smoothing, is 20.7 km/s. The integrated HI flux is obtained in making a slice exactly along the major axis of the galaxy providing a curve: $g(X)$ (full line in Fig 1 and Fig 2), where X is the radius along the major axis (corresponding to the X coordinate of the natural cartesian frame of the galaxy).

This curve, $g(X)$, is connected to the radial gaseous distribution $\Sigma_g(R)$ through an integral that can be inverted assuming low optical depth (Abel inversion formula), yielding:

$$\Sigma_g(R) = -\frac{1}{\pi} \int_R^{\infty} \left[\frac{\delta g(X)}{\delta X} \right] \frac{dX}{\sqrt{X^2 - R^2}} \quad (1)$$

The results are shown (dashed curve) in Fig 1 and

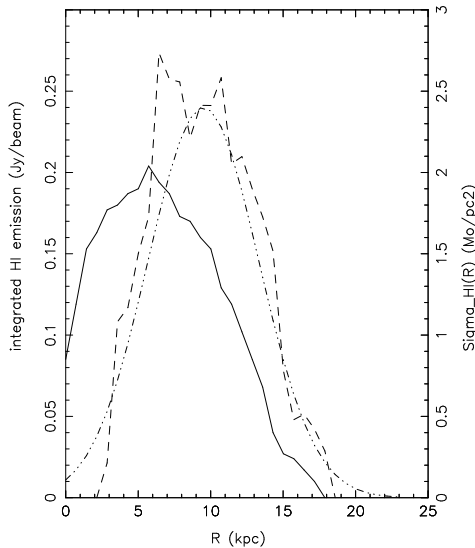


Fig. 1. The full line represents the observational integrated HI flux along the northern part of NGC 891 from r.m.s corrected zero moment map (in Jy/beam), while the dashed line is the surface gaseous density inverted from the integrated HI flux assuming low optical depth (in M_{\odot}/pc^2). The dot-dashed-dot gaussian curve represents the best fit of the axisymmetric gaseous density ($m = 0$), taking the southern part into account.

Fig 2. We note a good symmetry of the two curves inside $R_{HI,north}$ so that at first approximation we may write $\Sigma_g(R, \Theta) = \Sigma_g(R) = A_0(R)$. We fitted the gaseous radial distribution quite well with a gaussian law of characteristics given below. There are two uncertainties in this determination. First, the density formula (1) give negative gaseous densities in the very central parts ($R \leq 2$ kpc), since the derivative of the integrated flux curve is positive, such a behaviour of the $g(X)$ curve being due to an HI depletion in the center of the NGC 891 galaxy, which is quite often seen in the central parts of spiral galaxies. Second, the integrated flux has an intrinsic error due the non-infinite resolution, and we could observe that the density inversion formula was highly sensitive to local variations of the integrated flux curve. Assuming that the HI is distributed in a disk of radius $R_{HI,0}$ consists in replacing in the right term of (1) \propto by $R_{HI,0}$. It was interesting to find that the resulting radial density of the HI gas remains practically the same with or without this assumption (for $R_{HI,0} = 19$ kpc). This suggests that the

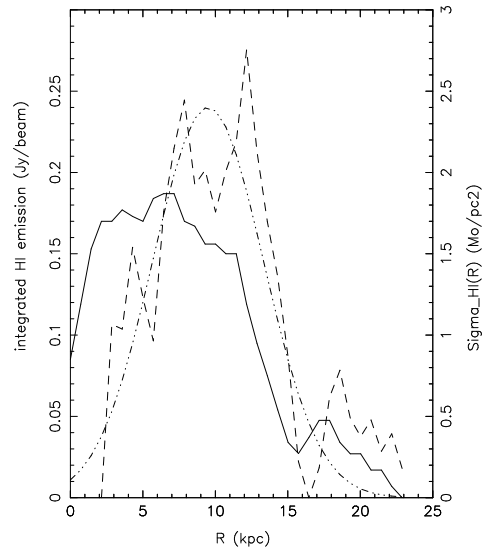


Fig. 2. Same as Fig 1 but for the southern part of NGC 891. We can observe a relatively good symmetry with the northern part until 5.5 arcmin (fitted with the gaussian curve), confirming the predominance of the axisymmetric mode.

high- Z gas surrounding the galaxy, which is probably located at large radii, is no more confined in the thin central HI disk, finally suggesting the presence of a warp along the line of sight, which is also the direction of integration of the HI flux. The gaussian law fitting axisymmetrically the northern and southern part of NGC 891 is:

$$A_0(R) = \frac{2.354\rho_{0,HI}}{\varrho_g\sqrt{2\pi}} \exp\left(-\frac{(R - R_g)^2}{2\varrho_g^2}\right) \quad (2)$$

with $R_g = 9.5$ kpc, $\varrho_g = 3.8$ kpc and $\rho_{0,HI} = 9.6 M_{\odot}/pc^2$. This fit of the axisymmetric radial gaseous distribution is quite sufficient for the rotation curve fit (next section), but for spectral cube modeling, we kept integrally the dashed curve representing the "real" $\Sigma_g(R)$, through stored data. We finally calculate the relation between the total HI mass and a gaussian surface density:

$$M_{HI} \approx 2\pi\rho_{0,HI}\varrho_g R_g \left(\sqrt{\frac{\pi}{2}} + 2\sqrt{\frac{2}{\pi}} \right)$$

This gives for $M_{HI} = 4.2 \cdot 10^9 M_{\odot}/pc^2$ (Rupen 1991 for $h = 0.75$) the value $\rho_{0,HI} = 8.0 M_{\odot}/pc^2$, in good agreement with our value of $\rho_{0,HI} = 9.6 M_{\odot}/pc^2$.

2.2. Modeling the warping of the disk

The warp is modelled as a vertical density wave of equation ($m=1$):

$$Z_{warp}(R, \Theta) = \Gamma(R) \cos(\Theta - \Theta_w) \quad (3)$$

The amplitude of this vertical wave, $\Gamma(R)$, is linearly parametrized but we also tested a law in R^2 (paraboloid):

$$\begin{aligned} \Gamma(R \leq R_w) &= 0 \\ \Gamma(R \geq R_w) &= \alpha_{lin}(R - R_w) \\ \Gamma(R \geq R_w) &= \alpha_{par}(R^2 - R_w^2) \end{aligned}$$

This parametrization corresponds to a flat disk's plane until a radius R_w , where the warp starts, and after follows the shape of the Γ function. We primarily included a global wave number for the warp wave (a $k_w R$ term in the cosine) but we finally neglected it for two reasons: firstly because the line of nodes of the warps are generally observed to be almost straight until large radii (Briggs, 1990) yielding that $k_w = 0$, and secondly because a twist of the line of nodes ($k_w \neq 0$), starting after some radius, is anyway hard to detect with spectral cube modeling (section 4). Simulating modes of warps embedded in dark matter halos, Sparke & Casertano (1988) frequently found linear solutions for the shape of the Γ functions. Briggs (1990) determined the tip angles (i.e. $\Gamma(R)$) of warps of a sample of 12 galaxies. Nearly all the features derived follow globally a linear or paraboloidal shape. Warps are generally observed to raise up at 3-5 exponential scale lengths of the light distribution, which corresponds more or less to the location of the optical radius. We show in Fig 11 a 3D model of NGC 891 which revealed to possess a warp of high amplitude, beginning at 2.5 exponential scale length (12 kpc).

2.3. Modeling the HI vertical distribution

It is expected from hydrostatic equilibrium that the HI layer is vertically distributed under a gaussian law only if the gas layer is much thinner than the stellar scale height. For the case of NGC 891, the exponential stellar disk has a vertical scale height $h_Z \approx 1.0$ kpc, and we determine in a further section, using our 3D spectral cube modeling, that the height of the inner gaseous layer H_0 is about 0.1 kpc so that we can assume a gaussian vertical distribution for the HI gas:

$$\rho_{gas} \propto \exp\left(-\frac{Z^2}{2Z_0(R)^2}\right) \quad (4)$$

If we write like Olling (1995) the Hydrostatic Equilibrium of the HI gas, under the assumption of Z-isothermality and axisymmetry, we obtain:

$$\sigma_Z^2 \frac{d \ln \rho_{HI}}{dZ} = -\frac{\partial \Phi_{galaxy}}{\partial Z} \quad (5)$$

INNER FLARING OF NGC 891

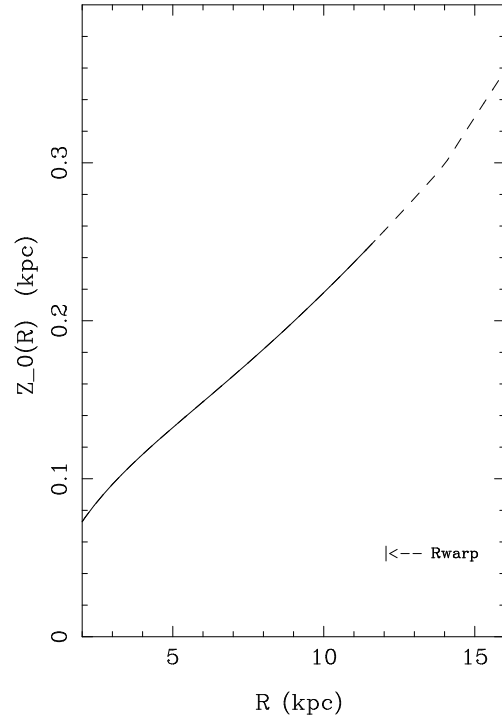


Fig. 3. NGC 891 flaring for a gaussian vertical distribution from the equation of hydrostatic equilibrium, using the rotation curve fit section results. This curve is invariant for Z between 0.1 and 0.5 kpc. R_{warp} is determined in the spectral cube modeling section.

so that inserting (4) in (5) yields:

$$Z_0(R) = \sigma_Z \sqrt{\frac{Z}{\frac{\partial \Phi_{galaxy}}{\partial Z}(R, Z)}} \quad (6)$$

Equation (6) is correct for small Z , and R smaller than R_w , since after this radius, the gas rises up in the warp. Equation (4) is then modified. Its form is also dependent on the dark matter model adopted: a disk-like dark matter distribution, following the HI layer, settles the gas in a potential well and the resolution of equation of the hydrostatic equilibrium will yield a solution in sech-2, while a spherical dark matter halo will provide a vertical force proportionnal to Z and thus a gaussian solution for the equation. But a sech-2 function and a gaussian have comparable behaviours for Z smaller than 1 kpc, so that in practice they cannot be separated. We thus adopted a gaussian representation:

$$\rho_{gas} \propto \exp\left(-\frac{(Z - Z_{warp}(R, \Theta))^2}{2Z_0(R)^2}\right) \quad (7)$$

We derive the galaxy potential of (6) from the rotation curve fit of next section. We determine using Fig 3:

$$Z_0(R \leq 12 \text{ kpc}) = 0.08 + 0.014R \text{ [kpc]}$$

We determine further (spectral cube modeling section) that this galaxy is warped relatively early in radius (beginning at about 12 kpc from the center of the galaxy, similarly to the Milky Way) so that an outer flaring cannot be determined only with a rotation curve fit. We observe that the inner flaring obtained above is almost linear as expected: many authors, (Pfenniger et al, 1994 or Olling, 1995) predicted such a behaviour. This leads us to consider for the spectral cube modeling section a warped gaussian HI vertical distribution with a flaring of the form:

$$\begin{aligned} Z_0(R \leq R_f) &= H_0 + \zeta_1 R \\ Z_0(R \geq R_f) &= H_0 + \zeta_1 R_f + \zeta_2 (R - R_f) \end{aligned} \quad (8)$$

where ζ_1 is the inner flaring coefficient and ζ_2 the outer flaring coefficient. The ζ coefficients are the slope of the flaring, they are dimensionless. The ζ_2 coefficient is naturally the most sensitive to the DMH geometry. This parameter can not be satisfactorily approached without modeling in 3 dimensions the warped neutral hydrogen layer.

3. Fit of the rotation curve

NGC 891 having a quasi edge-on orientation, and because of HI deficiency in its center, the HI rotation curve is inaccurate inside 8 kpc. The HI points are from Sancisi & Allen (1979), the relative error being of about 5 % after 8 kpc, in the flat region. A multi-component fit, although the method gives non-unique solutions, requires at least sufficiently good data, so that we considered for radii smaller than 8 kpc the CO curve provided by Garcia-Burillo et al (1992). NGC891 is expected to have a fast rotating nuclear disk (quite similarly to the Milky Way, see Dame et al, 1987), explaining why the CO rotation curve steepens to 250 km/s in 500 pc to fall at 225 km/s and stay constant up to 5 % at 225 km/s. We consider hereafter five components: a Toomre-Kuzmin nuclear disk, a Plummer bulge, a thick stellar disk, a gaseous contribution calculated for the previously derived radial HI surface density, and an ellipsoidal dark matter halo. The nuclear Toomre disk has a mass $M_{nuclear}$ and a scale-length $s_{nuclear}$. The Bulge spherical potential is classically

$$\Phi_B(R, Z) = \frac{-GM_B}{\sqrt{R^2 + Z^2 + s_B^2}}$$

and its rotational contribution is straightforward. The stellar disk is a thick exponential disk of density (van der Kruit, 1981):

$$\rho_*(R \leq R_{opt}, Z) = \rho_{0,*} \exp\left(-\frac{R}{h_R}\right) \exp\left(-\frac{Z}{h_Z}\right)$$

NGC 891 Rotation Curve Fit

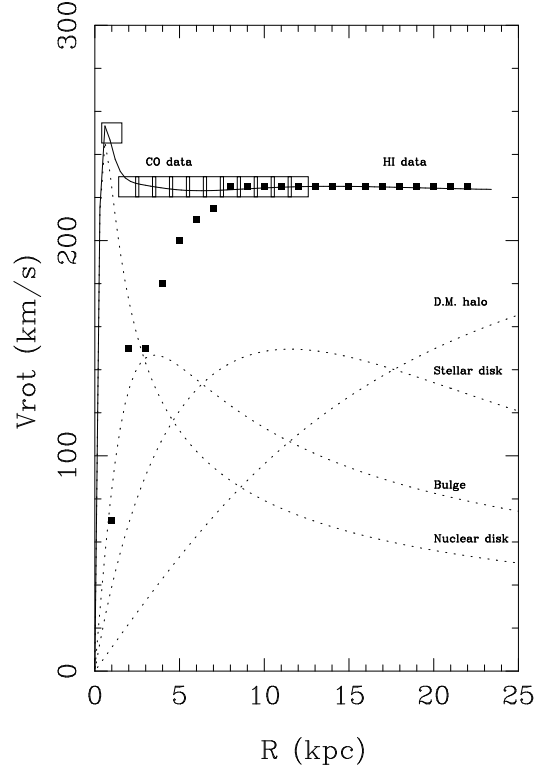


Fig. 4. Multicomponent fit of the rotation curve. Open squares are CO data from Garcia-Burillo et al (1992) while little full squares are HI data from Sancisi & Allen (1979). For this fit the dark component has a flattening of $q = 0.5$ and a core radius of 14 kpc. The HI contribution, negligible, is not drawn.

$$\rho_*(R \geq R_{opt}, Z) = 0.0$$

The value of h_Z and h_R are kept fixed since several previous studies have settled them with confidence (see Table 1). The disk potential is then (Sackett & Sparke 1990):

$$\Phi_*(R, Z) = -GM_* \int_0^\infty \frac{J_0(yR)[yZ_d e^{-|Z|/Z_d} - e^{-y|Z|}]}{(1 + h_R^2 y^2)^{3/2} (y^2 Z_d^2 - 1)} dy$$

We derive the contribution of the stellar disk to the rotation curve:

$$v_*^2 = -GM_* R \int_0^\infty \frac{y J_1(yR)}{(1 + h_R^2 y^2)^{3/2} (yZ_d + 1)} dy$$

We simulated also the equations of Casertano (1983) who includes explicitly the truncation of the stellar disk. But considering that the HI data stops before the optical radius in the north, and that some HI in the south is probably missing along the line of sight, truncation effects on the rotation curve are not expected to be visible, so that we adopted the formula of de Zeeuw & Pfenniger (refound by Sackett & Sparke, 1990).

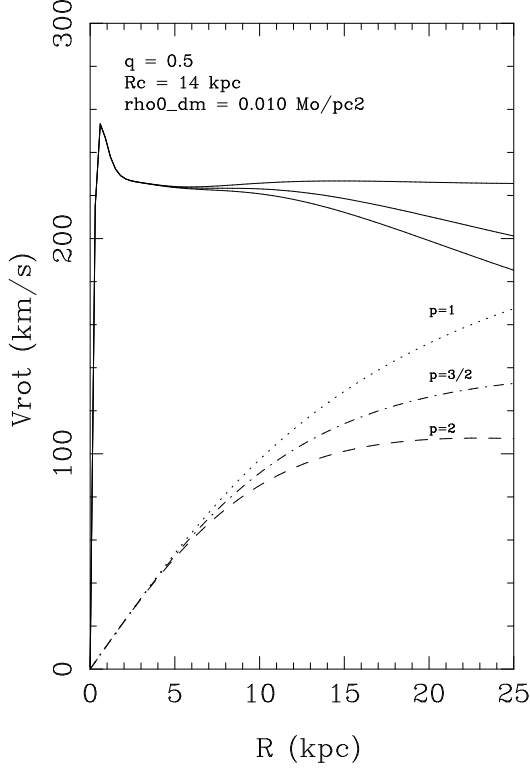


Fig. 5. The impact of modifying the dark matter density model on the rotation curve fit. Values of the parameters of the dark matter halo component are kept fixed, while only the power p changes.

We finally consider a dark matter component of isothermal, pseudo-ellipsoidal density:

$$\rho_{DMH} = \frac{\rho_{0,DMH}}{\left(1 + \frac{R^2}{R_c^2} + \frac{Z^2}{R_c^2 q^2}\right)}$$

This distribution generates the potential:

$$\Upsilon_{DMH}(R, Z) = 2\pi G \rho_{0,DMH} q R_c^2 \int_0^{\frac{1}{q}} \frac{\ln\left[1 + \frac{x^2}{R_c^2} \left(\frac{R^2}{\epsilon^2 x^2 + 1} + Z^2\right)\right]}{\epsilon^2 x^2 + 1} dx$$

where $\epsilon = \sqrt{1 - q^2}$. The halo contribution to the rotation curve is therefore:

$$v_{DMH}^2 = 4\pi G \rho_{0,DMH} q R_c^2 \int_0^{\frac{1}{q}} \frac{x^2 dx}{R_c^2 (\epsilon^2 x^2 + 1)^2 + (\epsilon^2 x^2 + 1) x^2 R^2}$$

which gives an asymptotic value, at large radii:

$$v_{DMH,\infty}^2 = 4\pi G \rho_{0,DMH} R_c^2 \frac{q \arccos q}{\sqrt{1 - q^2}}$$

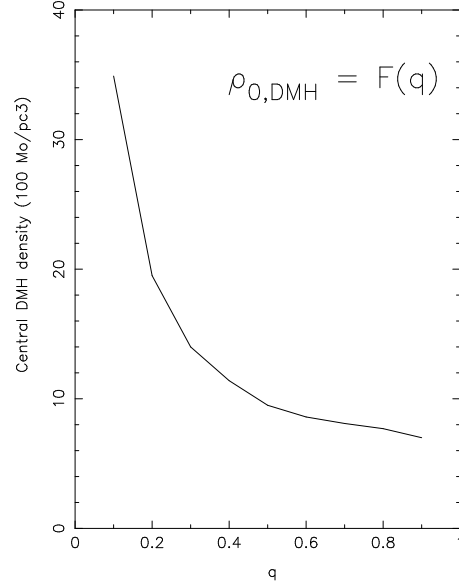


Fig. 6. The central density of the DMH as a function of its flattening, as found from the rotation curve fit.

An interesting particular case of dark matter density model is:

$$\rho_{DMH} = \frac{\rho_{0,DMH}}{\left(1 + \frac{R^2}{R_c^2} + \frac{Z^2}{R_c^2 q^2}\right)^p} \quad (p \geq 0)$$

The corresponding formula for the potential and rotation curve contributions are given in appendix C. The introduction of the power parameter p (we retrieve the normal dark matter density model for $p = 1$) is justified by the work of Lake & Feinswog (1989), who considered the possibility that $\rho_{DMH}(R, Z)$ is not necessarily in R^{-2} as it is currently assumed, the flatness of the rotation curves being also achievable for profiles in R^{-3} and even R^{-4} (corresponding respectively to $p = \frac{3}{2}$ and $p = 2$). We simulated both values of p at the end of this section, in order to estimate the implication on the amount of dark matter required (Fig 5).

Taking the gaussian fit of HI radial distribution, we derive using formula 2-160 of BT87 the HI contribution:

$$v_{HI}^2 = -G \rho_{0,HI} R \int_0^\infty x J_1(xR) \left[\int_0^\infty \exp\left(-\frac{(R - R_g)^2}{2\sigma_g^2}\right) J_0(xy) y dy \right] dx$$

In fact, the HI contribution to the rotation curve revealed to be negligible: in the outer parts, it is of the same order than the nuclear disk contribution. Inserting the HI contribution modifies the dark mass required of about 2 %, less than the error made in ignoring the stellar truncation. The halo parameter R_c can be somehow constrained using the $[M/L]$ ratio of the stellar disk. Several simulations were made for several halo core radii: in each case the flatness of the rotation curve could be obtained, but for R_c values lower than 12 kpc, the disk mass had to be more and more severely decreased. The disk mass required for $R_c = 14$ kpc is $M_\star = 7.7 \cdot 10^{10} M_\odot$ yielding a mass-to-light ratio in blue color of $[M/L]_{\star,B} = 7.1 M_\odot/L_\odot$, in excellent agreement with the value of 7.0 found by van der Kruit (1981). For $R_c = 8$ kpc, keeping the flatness of the curve requires the disk mass to be $M_\star = 5.4 \cdot 10^{10} M_\odot$ providing a mass-to-light ratio of 4.9 which is far too low (Bottema et al 1991). So that we settle the halo core radius at about 14 ± 2 kpc.

The mass of dark matter enclosed in an oblate ellipsoid of half major axis d and flattening q is given by:

$$M_H(< d) = 4\pi\rho_{0,DMH}R_c^2q\left[d - R_c \arctan\left(\frac{d}{R_c}\right)\right]$$

Considering the dark mass enclosed within 30 kpc, in a semi-flattened ellipsoid of $q=0.5$, of core radius $R_c = 14$ kpc, we calculate that $M_H = 17 \cdot 10^{10} M_\odot$.

The simulation of the generalized dark matter densities with $p = \frac{3}{2}$ and $p = 2$ modifies drastically the results. We show in Fig 5 the alteration of the dark matter contribution for the same halo parameters, but for different values of p . Non-isothermal values of p (i.e. $p \geq 1$) require much greater dark matter central densities, and modifies the stellar disk mass severely. We keep $p = 1$ for the rest of the article. We finally remark that fitting the HI data only (i.e. without considering the inner CO data), leaves unchanged the dark matter component parameters. The results of our best fit (Fig 4) are quoted in Table 1. We plot in Fig 6 the relation between $\rho_{0,DMH}$ and q .

4. Numerical method

4.1. The code

The construction of synthetic spectral cubes requires the use of many parameters, among which six are considered as free parameters: the warp parameters α_w, R_w and the flaring parameters $R_f, H_0, \zeta_1, \zeta_2$.

A rapid code is thus necessary. We separate the density model building from the kinematics (velocity sampling). To build the density model, and to project it, we choose to distribute randomly particles in space: this technique is much more efficient (in terms of CPU time) than a 3D cube construction, for a given spatial resolution; this is due to the fact that the 3D cube has a very little volume filling factor, therefore the number of particles required

Table 1. Results of the rotation curve fit.

quantity	fitting value
$s_{nuclear}$	$= 0.4 \text{ kpc}$
$M_{nuclear}$	$= 1.5 \cdot 10^{10} M_\odot$
s_B	$= 2.5 \text{ kpc}$
M_B	$= 3.2 \cdot 10^{10} M_\odot$
h_Z	$= 0.99 \text{ kpc}$
h_R	$= 4.9 \text{ kpc}$
M_\star	$= 7.7 \cdot 10^{10} M_\odot$
$[M/L]_{\star,B}$	$= 7.1 M_\odot/L_\odot$
R_c	$= 14 \text{ kpc}$
$M_H(q = 0.5, R \leq 30 \text{ kpc})$	$= 17 \cdot 10^{10} M_\odot$
$\rho_{0,DMH}(q = 0.1, R_c = 14 \text{ kpc})$	$= 0.0349 M_\odot/pc^3$
$\rho_{0,DMH}(q = 0.2, R_c = 14 \text{ kpc})$	$= 0.0195 M_\odot/pc^3$
$\rho_{0,DMH}(q = 0.3, R_c = 14 \text{ kpc})$	$= 0.0140 M_\odot/pc^3$
$\rho_{0,DMH}(q = 0.4, R_c = 14 \text{ kpc})$	$= 0.0114 M_\odot/pc^3$
$\rho_{0,DMH}(q = 0.5, R_c = 14 \text{ kpc})$	$= 0.0095 M_\odot/pc^3$
$\rho_{0,DMH}(q = 0.6, R_c = 14 \text{ kpc})$	$= 0.0086 M_\odot/pc^3$
$\rho_{0,DMH}(q = 0.7, R_c = 14 \text{ kpc})$	$= 0.0081 M_\odot/pc^3$
$\rho_{0,DMH}(q = 0.8, R_c = 14 \text{ kpc})$	$= 0.0077 M_\odot/pc^3$
$\rho_{0,DMH}(q = 0.9, R_c = 14 \text{ kpc})$	$= 0.0070 M_\odot/pc^3$

are much lower than the number of cube cells, and various 3D rotations are then much quicker.

4.1.1. Rendering the HI 3D geometry

The computational form of the model density is:

$$\rho_{HI}(R, \Theta, Z) = \Sigma_g(R) \exp\left(-\frac{(Z - Z_{warp}(R, \Theta))^2}{2Z_0(R)^2}\right)$$

where $\Sigma_g(R)$ has been derived from section 2.1, approximated by the equation (2), $Z_{warp}(R, \Theta)$ is the warp wave described by equation (3) and the flaring of the gas is included in $Z_0(R)$ through the ζ -linear law of equation (8). We generate N particles $[x(i), y(i), z(i); i \in 1, \dots, N]$ from the density model above, on which we operate a spatial rotation $\mathfrak{R}_{3D} = \mathfrak{R}(I, j) \circ \mathfrak{R}(PA, k)$, where "I" is the inclination of the galaxy and "P.A." its position angle, thus projecting the set of particles on the sky plane with the orientation angles of the real galaxy.

4.1.2. Spectral sampling and synthetic spectral cube

A velocity is associated to every particle in the cube. The rotational velocity $V_{rot}(R)$ is interpolated from the previously fitted rotation curve. We project the velocities onto the plane of the sky to get radial velocities:

$$V_{los} = V_{sys} + V_{rot} \sin I \cos \Theta$$

Having a set of particles and the associated radial velocities, we now sample this 4 dimensions space $[x, y, z, V]$ according to our original NGC 891 spectral cube. This

sampling is done according to a central (systemic) velocity and a fixed increment $\Delta V = \sqrt{\Delta V_{chan}^2 + \sigma_{HI}^2}$ to get channel maps (this assumes an isotropic dispersion σ_{HI}). For our test-galaxy, ΔV_{chan} is 20.7 km/s. The procedure of the construction is the following. For the Nst channel map $V_N = V_{sys} + N \times \Delta V_{chan}$, we fill a temporary pixel cube with the spatially rotated particles in multiplying this geometric cube by a gaussian in V_N , centered on our previously calculated V_{los} , and of dispersion ΔV . We finally sums the flux perpendicularly to the plane of the sky to obtain a channel map (the Nst). We finally loop over N (in our case from 5 to 25, 15 corresponding the systemic velocity) to get an entire modelled spectral cube $[X, Y, V_{los}]$. The last operation consists in convolving every pixel of the spectral cube by gaussians of FWHM corresponding to the synthesized beam of the VLA observations ($20'' \times 20''$ for NGC 891).

4.1.3. Application of the code

The random launching of particles in space takes negligible CPU, in front of the kinematics part. The dimensions of the cube is $300 \times 300 \times N_{chan}$, yielding a spatial resolution of 1 pixel = 3 arcseconds (=147 parsecs), but the technique allows to build channels one by one, and only some of the total number of channels ($N_{chan}=30$) are computed for the whole set of free parameters. In practice, 6 channel maps (whatever the number of particles) are sampled and beam-smoothed from one spectral cube in about 30 seconds on one processor of a CONVEX 3440.

Spatial resolution is the dominant parameter to the control of CPU time. The observed HI cube of NGC 891 displays 30 channels, 24 of them having significant flux (channels 2 to 25), the center being the systemic velocity channel 15 (see Rupen 1991 for the mosaic figure of the 30 channels). To restrict at maximum the CPU, we modelled every two channels. The inclination of this galaxy has been estimated several times in the literature, leading to a firm lower limit $I \geq 88.6^\circ$ (Rupen, 1991). The inclination is thus kept constant at 89.0 degrees since the uncertainty on its value is too small (± 0.3 degree) to assign I to be a free parameter. In the same way, the position angle was fixed to 23.5 degrees (Garcia-Burillo et al 1992). Van der Kruit (1981), using Velocity-Position diagrams of models, concluded to a constant velocity dispersion of the gas (assumed isotropic) of 10.0 km/s.

4.1.4. The experiments

A library of models exploring the free parameters are compared to the HI observations (in figures 7, 8 and 9). With linear contours centered on the half-intensity of the channels, the spectral cube of NGC 891 (whether south or north) do not show any feature resembling to what Olling nicely calls "butterfly wings", which are characteristic of HI flaring and warp. To make weak structures at large

height above the plane emerge, contours have to be adequately selected, as in Fig 7, which presents flaring and warped HI layers.

Our first idea was that the surrounding high-Z gas (the low intensity features surrounding the disk up to several kpc height, visible in the channel maps "north NGC 891" of Fig 7, Fig 8 and Fig 9) could be interpreted as a warp in the line of sight, and so we fixed the value $\Theta_w = 90^\circ$. We used to test this configuration the northern part of the spectral cube since no HI extension along the major axis is required.

The radial distribution of the HI gas is assumed to be the dashed curve found in section 2.1. The gaussian model approximating this dashed curve is used later, for the detection of a spiral pattern; from that the axisymmetric mode is globally determined. We see in Fig 7, Fig 8, Fig 9 samples of our intensive construction of spectral cubes. We vary nearly all possible parameters, intending to show what transformations on the 2D flux distribution correspond to the variation of each parameter. The first seven synthetic cubes shown in Fig 7 are presented to observe the 2D flux transformations that take place for extreme values of parameters. We do not search for this first sequence to obtain cubes that are close to observations, but rather to build a library of models.

x1: $\alpha_{lin} = 0, \zeta_1 = 0, \zeta_2 = 0, H_0 = 0.05$ kpc.

x2: $\alpha_{lin} = 0, \zeta_1 = 0, \zeta_2 = 0, H_0 = 0.9$ kpc. This x2 synthetic cube displays a too high HI constant thickness. By comparison with the observed cube, the average value is more towards low values ($H_0 \approx 0.1 - 0.5$ kpc).

x3: $\alpha_{lin}(R_w = 5$ kpc) = 0.4, $\zeta_1 = 0, \zeta_2 = 0, H_0 = 0.4$ kpc. This synthetic cube displays a warp of too high amplitude, generated too early. We clearly see that the HI disk flux of the observations is totally different.

x4: $\alpha_{lin}(R_w = 1$ kpc) = 0.2, $\zeta_1 = 0, \zeta_2 = 0$. The effect of decreasing the amplitude of the warp, makes its "wings" to join. The double "symmetric" holes of the channel 15 are sufficient to rule out this model.

x5: $\alpha_{lin}(R_w = 3$ kpc) = 0.08, $\zeta_1 = 0, \zeta_2 = 0$. For very low amplitudes of the warp, we reconstruct the observed HI disk: in fact, there is no more high-Z gas surrounding the disk, as is observed.

x6: $\alpha_{lin}(R_w = 10$ kpc) = 1., $\zeta_1 = 0, \zeta_2 = 0$. We show here a warp generated at 10 kpc, further than before. We observe the emergence of high-Z gas surrounding the central HI disk. We also notice that R_w is easy to locate in the way that the gas after R_w is displaced, inducing a "truncature" of the outer HI central disk. In particular, the 25th channel is very sensitive to that modification. We conclude from comparison with observations that the warp is prob-

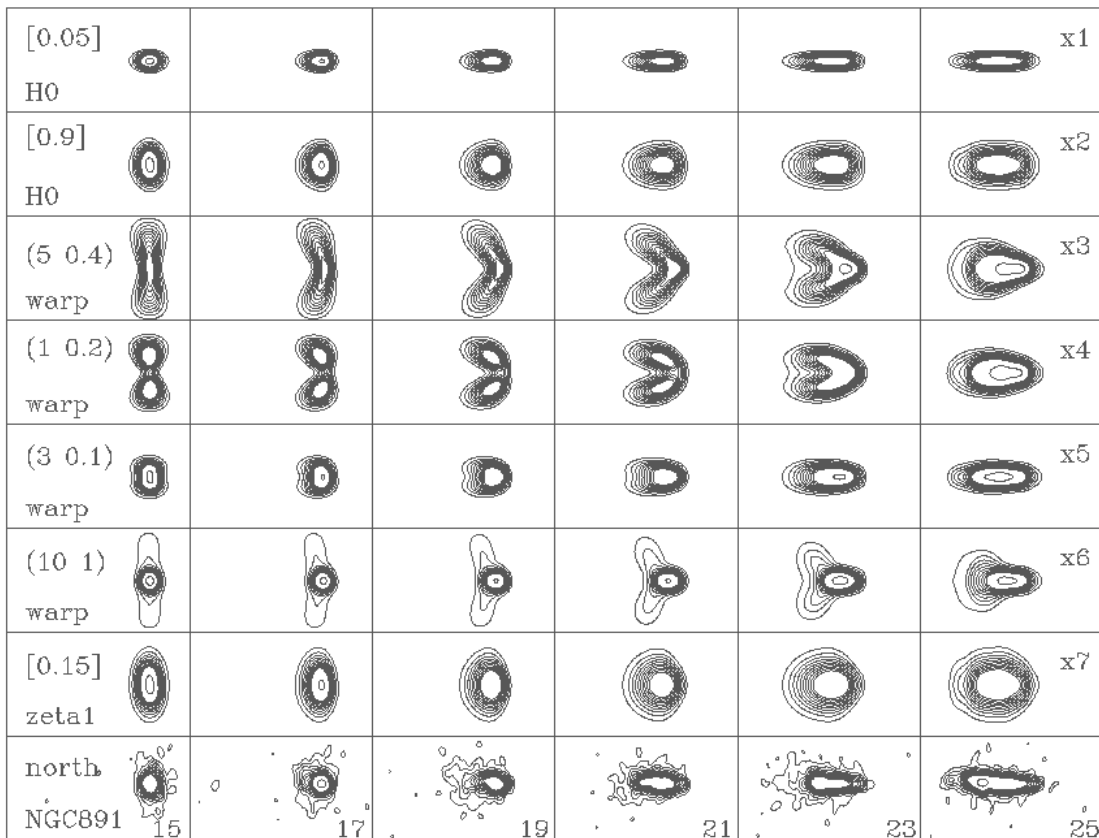


Fig. 7. Library of models: we present here 7 synthetic spectral cubes x1 to x7 (to be compared with the original spectral cube "north NGC 891" displayed as the 8th cube). The same contours are used for every cube: 0.002:0.024:0.002 and 0.036 Jy/beam. The channels presented here are the systemic channel 15 (535 km/s), and the channels 17 (575 km/s), 19 (620 km/s), 21 (660 km/s), 23 (705 km/s), 25 (745 km/s).

ably generated a little bit further, around $R = 12$ kpc.

x7: $\alpha_{lin} = 0$, $\zeta_1 = 0.15$, $\zeta_2 = 0$, $H_0 = 0.1$. We observe now the location of an exaggerated inner flaring. This inner flaring of 0.15 is about ten times the inner flaring expected with the hydrostatic equilibrium of the gas (section 2.3).

x8: $\alpha_{lin} = 0$, $\zeta_1 = 0$, $\zeta_2 = 0.6$, $R_f = 12$, $H_0 = 0.1$. Testing the outer flaring coefficient at an abnormal value of 0.6. We observe that there are clear 2D effects induced.

We now try to combine these results to build a sequence of cubes closer to the observed one.

x9: $\alpha_{lin}(R_w = 10) = 1$, $\zeta_1 = 0.02$, $\zeta_2 = 0.02$, $H_0 = 0.4$. A flaring warp. We kept the warp parameters of cube x6, in adding a flaring of the gas. We notice that the flaring densifies the contours following the warp along the line of sight, so that even not very well constrained intrinsically, the flaring can be approached.

The main problem when we observe the cube x9 in com-

parison to the observed cube is that the extreme channel maps (23 and above all 25) are in every of our models surrounded by high-Z gas, while they are not in the observed cube. The observed channel map 25 is very thin, so that it appears necessary that the particles in the warp rotate at a different speed than the HI in the disk plane. This was already noticed by Swaters et al (1997), and interpreted as non-cylindrical rotation of the HI disk, due to energetic star-formation. To estimate quantitatively the amount of non-cylindrical rotation, we adopt a simple kinematical model: we assign a rotational velocity of high-Z particles lower than in the plane by a free factor (between 1 and 2), for heights greater than the inner disk HI thickness, typically 150 parsecs.

x10: Simulating high-Z particles as rotating at $V_0/2$, where V_0 is the "plateau" speed of the rotation curve in the plane (i.e. 225 km/s). The parameters for this cube are: $\alpha_{lin}(R_w = 9) = 1.3$, $\zeta_1 = 0.02$, $\zeta_2 = 0.02$, $H_0 = 0.4$. We observe that the high-Z gas concentrates around the center channels 15, 17, 19 leaving the extreme channel 23, 25 without high-Z gas, which is one of the characteristics

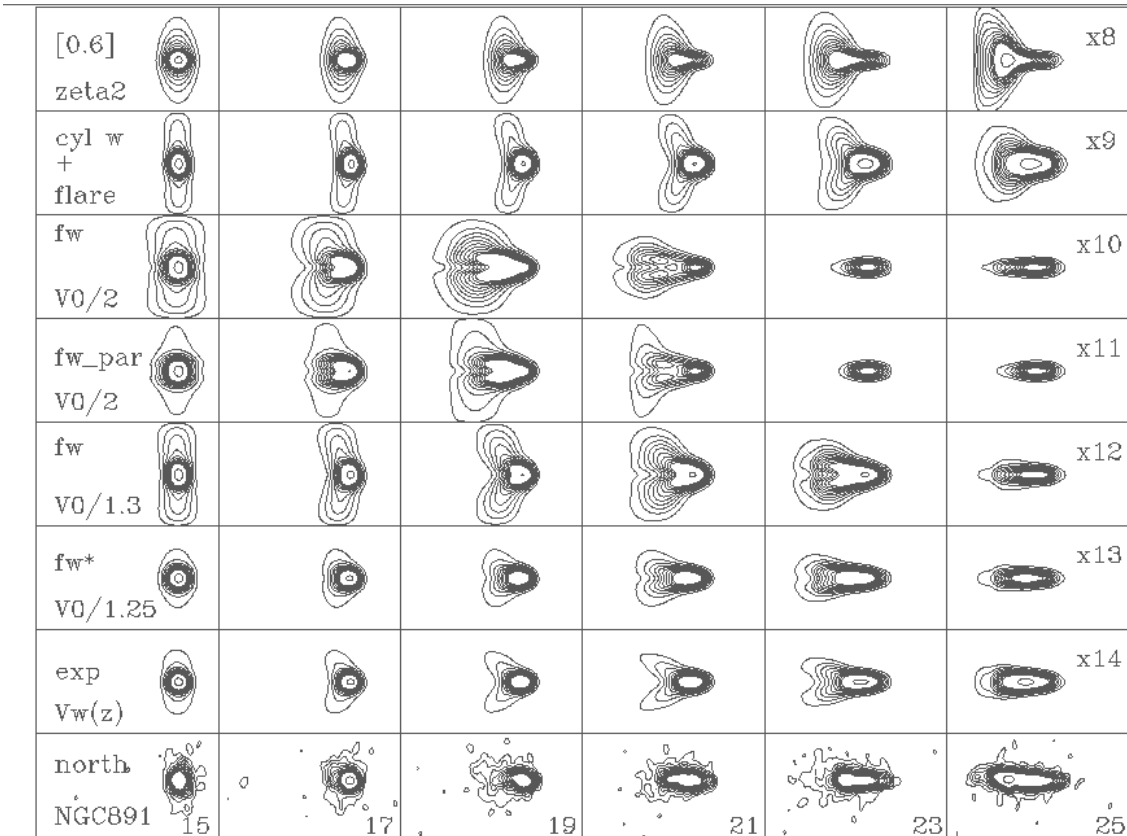


Fig. 8. We present 7 synthetic spectral cubes x8 to x14 ”converging” towards our best fits x13 and x14 (to be compared with the corresponding channels ”north NGC 891”). The same contours are used in every cube: 0.002:0.024:0.002 0.036 Jy/beam.

of the observed spectral cube.

x11: same parameters but now with a parabolic warp instead of linear, of same maximum height as the previous cube x10. We observe by comparison that a linear warp makes ”round” waves instead of ”square” waves obtained with a Γ function in R^2 . A linear warp seems closer to the observations. We also can appreciate that the warp is generated too early, truncating the end of the central HI disk (visible in particular for the 25th channel).

x12: same as x10, but with $V_{warp} = V_0/1.3$. We see that it is possible to make the 25th channel very thin, as in the observed cube. A velocity ratio of 1.3 shows up to be closer to the observations than the velocity ratio of 2 of the previous model cube since it allows the 23rd channel to have high-Z gas.

x13: A more accurate cube with $V_{warp} = V_0/1.25$. We have here the definitive values of the geometric parameters:

$$\alpha_{lin}(R_w = 12) = 0.8, \zeta_1 = 0.02, \zeta_2 = 0.02, H_0 = 0.1$$

x14: We refine the kinematical description of the warp

behaviour detected. Instead of considering that the warp cylindrically rotates, we test now a vertical velocity gradient with an empirical ”exponential” law. The model becomes:

$$V_{los} = V_{sys} + V_{rot} \sin I \cos \Theta \exp(-0.1|Z|)$$

Regarding the hypothesis of the model (as the decoupling R-Z of the model) and the fact that the radial distribution of the gas in section 2.1. is not perfect, we consider as successful (with the 2 last synthetic spectral cubes x13 and x14) our goal to rebuild the observations.

We try now to simulate the non-symmetric features observed in NGC 891 cube. We consider the sum of the R-gaussian axisymmetric mode $A_0(R)$ determined in section 2.1 and an $m = 2$ harmonic term. We generate the spiral after the HI central depletion of the galaxy, at about 2 kpc, let it develop and make it decrease in $1/R$ after a radius R_{spir} . The formulation in the model is the following

$$\begin{aligned} \Sigma_g(R \leq 2 \text{ kpc}) &= 0 \\ \Sigma_g(R \leq R_{spir}) &= A_0(R) + A_2 \cos(k_2 R - 2(\Theta - \Theta_2)) \end{aligned}$$

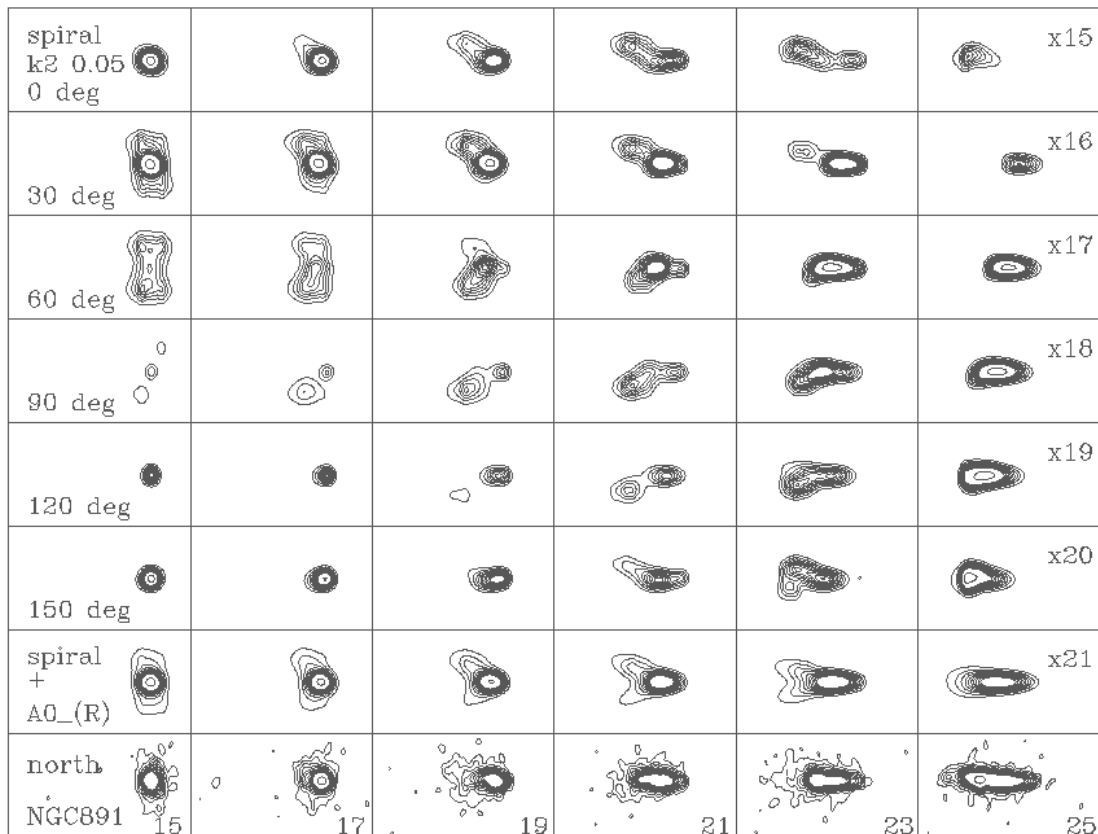


Fig. 9. Spiral cubes: 6 synthetic spectral cubes representing an $m = 2$ spiral mode simulated alone, with a fixed wave number ($k_s = 0.05$) and a varying line of nodes (from 0° to 150°). The height reached by the spiral has been a bit amplified in settling R_{spir} at 15 kpc, that is 3 kpc more than R_w . We suppose that R_{spir} is in reality of order R_w . The seventh cube (x21) is a combination of a gaussian $A_0(R)$ and an $m = 2$ harmonical mode with $\Theta_2 = 30^\circ$. The same contours are used in every plot: 0.002:0.024:0.002 0.036 Jy/beam.

$$\Sigma_g(R > R_{spir}) = A_0(R) + \frac{A_2 \cos(k_2 R - 2(\Theta - \Theta_2))}{R - R_{spir}}$$

where k_2 is the global wave number, Θ_2 the line of nodes of the spiral pattern, and where A_2 is of small magnitude in comparison to $A_0(R)$. Computing alone (i.e. $A_0(R) = 0$) the $m = 2$ term in our spectral cube code (Fig 9), we could associate the external "torsion" of the gas, unexplained with our symmetric models, to an $m = 2$ warped spiral. We kept the flaring warp parameters found in the axisymmetric mode construction. The velocity of the spiral arms is calculated in Appendix B and is implemented in the code. Synthetic cubes x15 to x20 show an $m = 2$ spiral with $k_2 = 0.05$ and regularly varying line of nodes (from 0° to 180°). It is important to notice that R_{spir} is found greater than R_w (of about 3 kpc), explaining the asymmetric features of the high-Z gas: the spiral is raised by the warp before its density vanishes, so that a non-negligible quantity of matter is asymmetrically placed in the line of sight, at heights corresponding to the warp wave.

x21: This synthetic cube is the superposition of the axisymmetric gaussian density found in section 2.1., with an $m = 2$ spiral ($k_2 = 0.05$, $\Theta_2 = 30^\circ$). We observe unambiguously that a spiral can reproduce the observed asymmetry. It is noteworthy that the gaussian HI density is only an approximation in front of the "real" $\Sigma_{HI}(R)$ stored in buffers: the 25th channel, as an example, is less well fitted (see x14 for comparison).

4.1.5. Conclusion on the HI 3D distribution according to our model

Several hundreds of synthetic cubes under the configuration of a warp along the line of sight ($\Theta_w = 90^\circ$) were finally built. Most parameters induce typical and particular 2D effects:

- 1- a flaring warp along the line of sight makes "butterfly-shapes" that can be associated to the observed high-Z features of the gas.
- 2- a flaring also thickens regularly the central HI disk, a behaviour which is clear for the 23rd channel of NGC 891. Combinations step by step of the parameters succeeded

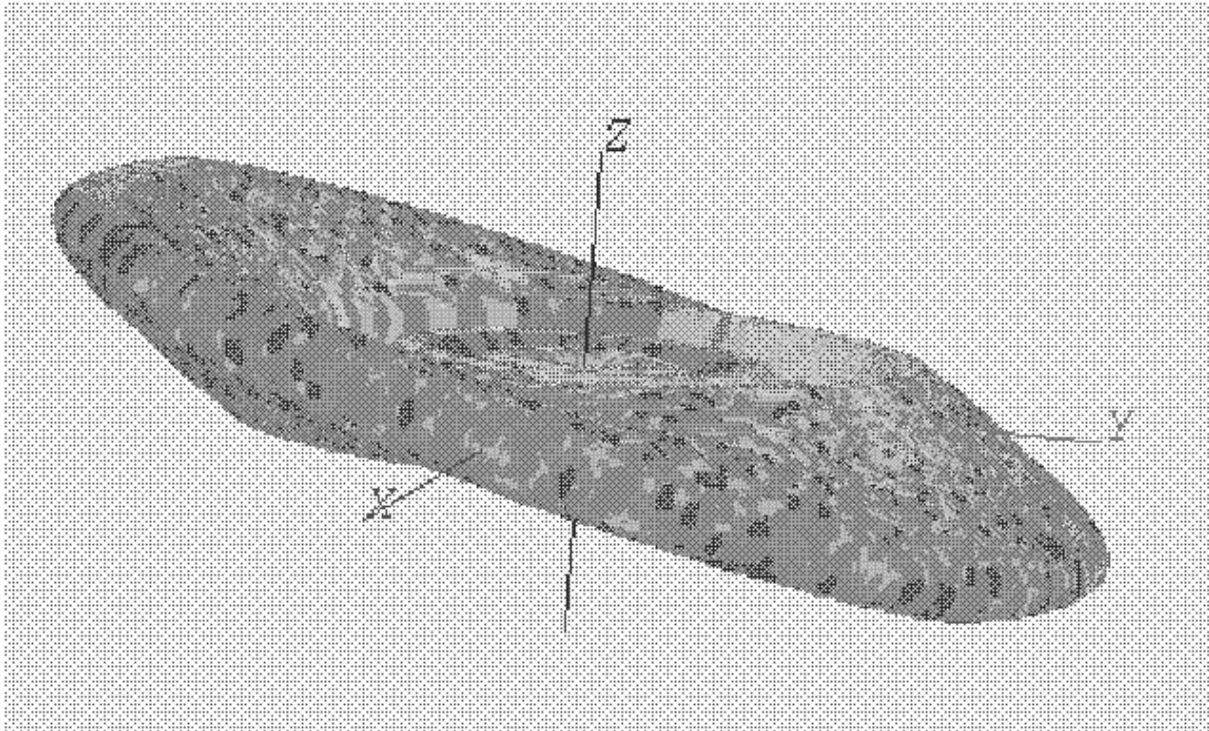


Fig. 11. The 3D HI isodensity contour of NGC 891 from a synthesis of our results. The radial distribution comes from section 2.1 while the vertical gaussian distribution has the parameters found in the spectral cube modeling: $H_0 = 0.1$ kpc, $\zeta_1 = \zeta_2 = \zeta = 0.02$. The warp appears clearly along the Y axis accordingly to $\Theta_w = 90^\circ$.

to reproduce most of the features observed in the original spectral cube of NGC 891. The radius where the warp begins, for instance, is very sensitive: we are able to set it with a good confidence at 12 ± 0.3 kpc. The amplitude of the warp, α_{lin} , is about 0.7 to 0.8, depending on the true pattern of the $m = 2$ spiral. The most important result is that we found possible to constrain the flaring (see synthetic cubes with varying ζ_1, ζ_2 coefficients). Let us summarize the other deductions:

1- The flaring found after modeling in 3D is of the same order than the value estimated using the potential derived from the results of the rotation curve fit section (section 2.3).

2- Modeling with success the gas in 3D requires the use of every channel. The central channels were needed in our case to constrain the amplitude of the warp, and the extreme channels 23 and 25 were needed to detect the kinematical behaviour of the warp wave. In particular, the channels 15 and 23 showed to be the most sensitive to the flaring coefficients.

3- The kinematical behaviour of the warp appeared to be dominated by an important velocity gradient. If there is indeed a strong warp, so that the HI gas reaches a height of a few kpc above the plane at a radius of 20 kpc, then we expect a significant rotational velocity gradient perpendicular to the plane. This gradient is of much larger amplitude that the simple gradient expected from non-

cylindrical rotation (appendix A). It is due to the fact that the gas orbits in inclined planes (as in the tilted ring model of warps) while the bulk of the matter, represented by the stars, is flattened in the plane. The periodic orbits in the tilted plane are not circular, but elongated, with their minor axis in the plane of the galaxy. Their tangential velocity is then larger on the minor axis (i.e. in the plane) than on their major axis (at their apocenter, at their maximum height above the plane). This produces a z-velocity gradient of the measured rotational velocity. To compute the order of magnitude of this gradient, we have taken our model of the NGC 891 potential, including the bulge, nuclear disk, and mainly the exponential stellar disk. We also introduced the dark halo, with variable flattening, but this had only a small influence on the orbits between 10 and 20 kpc. To find the closed elongated orbits in the tilted planes, we then used the shooting method, as in the computations of the kinematics of polar rings (e.g. Sackett et al 1994, Combes & Arnaboldi 1996). We discovered that, for all orbits between 10 and 20 kpc average radii, the average ellipticity of the orbits is $\sim 12\%$, and the tangential velocity on the major axis is $\sim 30\%$ less than that on the minor axis, for a tilt of the plane of 20° (see figure 10). By comparison, the expected non-cylindrical z-velocity gradient for the same tilt is of the order of 10% only. Assuming such a warp for NGC 891, with a line of nodes coinciding with the line of sight, permits us to fit the

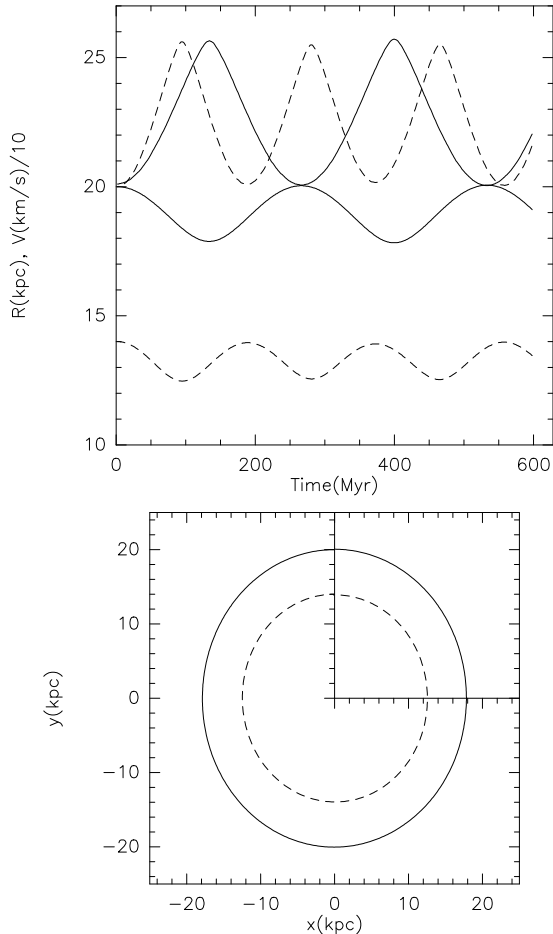


Fig. 10. Computation of the orbits with the shooting method; *bottom*: shape of closed orbits launched at $R=14$ and 20 kpc, in a plane tilted by 20° from the equatorial plane, the major axis is along Ox ; *top*: Time evolution of the radius and velocity of the two orbits, one launched at 20 kpc (full line), the other at 14 kpc (dashed line). The largest relative variations are those of the velocity (about 30%)

observations quite nicely. The HI above the plane on the minor axis is taken into account, with a rotational velocity less than in the plane, which removes high- Z HI from the extreme velocity channels. The high- Z HI is then confined in channels closer to the systemic velocity, as shown in Fig 8. We can note a posteriori that this effect can produce an over-estimation of the rotational velocity at large radii, since the velocity in the plane is higher than it should be for circular orbits. It is then possible that the true rotation curve of NGC 891 is not flat, but slightly falling down at large radii.

The results of this spectral cube modeling are listed below:

$$\begin{aligned} \Theta_w(NGC\ 891) &\approx 90^\circ \\ H_0(NGC\ 891) &\approx 0.1\ (kpc) \\ \zeta_1(NGC\ 891) &\approx 0.02 \\ R_f(NGC\ 891) &\approx 12\ (kpc) \\ \zeta_2(NGC\ 891) &\approx 0.02 \\ \alpha_{lin}(NGC\ 891) &\approx 0.6 - 0.8 \\ R_w(NGC\ 891) &= 12\ (kpc) \end{aligned}$$

For comparison, we collected the HI parameters for the Milky Way, most of them coming from Merrifield (1992):

$$\begin{aligned} \Theta_w(MW) &\approx 80^\circ \\ H_0(MW) &= 0.1\ (kpc) \\ \zeta_1(MW) &\approx 0.04 \\ R_f(MW) &\approx 16\ (kpc) \\ \zeta_2(MW) &\approx 0.08 \\ \alpha_{lin}(MW) &\approx 0.3 \\ R_w(MW) &= 12\ (kpc) \end{aligned}$$

We can note significant differences between the two galaxies. Although they both have the same constant HI layer thickness and both have a warp beginning at the same radius (12 kpc). The warp of NGC 891 is however much higher in amplitude (reaching 6 to 8 kpc height at $R=22$ kpc, as the Milky Way's warp raises up to 4 kpc height at $R=25$ kpc). Also the flaring of NGC 891 is less by a factor 2 in comparison with the Milky Way. We have plotted (Fig 11) a perspective view of our best fit model of NGC 891.

5. The flattening of an ellipsoidal DMH using the outer flaring of the HI layer

The fit of the rotation curve was made with an ellipsoidal dark matter density model. This axisymmetric dark matter density model has the advantage to generate an axisymmetric potential that simplifies substantially the set of hydrodynamical and gravitationnal equations formed by the hydrostatic equilibrium of the HI gas and the Poisson equation.

Following Olling (1995), the projection on the Z axis of the Jeans Equation becomes the equation of Hydrostatic Equilibrium:

$$\frac{d(\rho(Z)\sigma_Z^2(Z))}{dZ} = \rho(Z)F_Z(Z) - \frac{1}{R} \frac{\partial(R\rho\sigma_{RZ}^2)}{\partial R} \quad (9)$$

where the term in Θ has been eliminated due to the azimuthal symmetry of the gaseous distribution ($m = 0$ is overwhelming). For Z/R small ($Z \geq 0$) the tilt of the gaseous velocity dispersion ellipsoid σ_{RZ} is approached by (BT87):

$$\sigma_{RZ}^2 \approx (\sigma_R^2 - \sigma_Z^2) \frac{Z}{R}$$

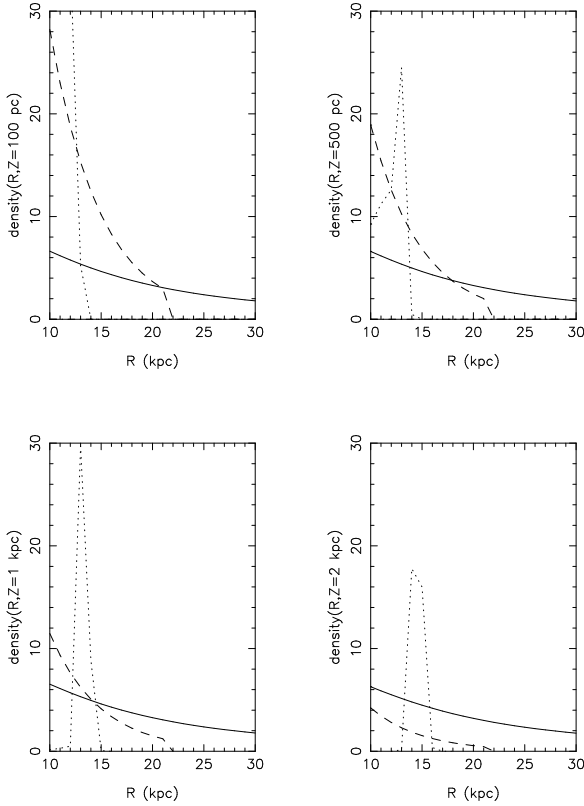


Fig. 12. We show here the densities of each component of the galaxy, for different heights, and for radii corresponding to the outer parts. The parameters of these components are found from the rotation curve fit. The dotted curve points out the HI density vertically distributed ($H_0 = 0.1 \text{ kpc}$, $\zeta = 0.02$) as a gaussian following the warp wave ($\alpha_{lin}(R_w = 12 \text{ kpc}) = 0.8$). The disk and DMH densities are dashed and full curves respectively. The DMH has fixed parameters: $R_c = 14 \text{ kpc}$ and $q = 0.5$. The bulge density for $R \geq 10 \text{ kpc}$ is totally negligible (and do not even appear in the graphs). The dark matter density term dominates after 20 kpc. Densities are in units of $0.001 M_\odot/\text{pc}^3$.

that we replace in the equation. Although σ_Z cannot be measured at large R , observations of face-on external galaxies show little or no variation of the Z -dispersion with R (e.g. Dickey et al, 1990). Assuming the vertical and radial velocity dispersion of the HI gas independent of R :

$$\sigma_Z^2 \frac{d \ln \rho_{HI}}{dZ} + (\sigma_R^2 - \sigma_Z^2) \frac{Z}{R} \frac{d \ln \rho_{HI}}{dR} = -\frac{\partial \Phi_{galaxy}}{\partial Z} \quad (10)$$

where

$$\Phi_{galaxy} = \Phi_{bulge} + \Phi_\star + \Phi_{HI} + \Phi_{DMH}$$

Parallel to the hydrostatic equation (10), let us write the Poisson equation for $R \geq 8 \text{ kpc}$ (flat region of the rotation curve). Deriving with respect to R the equation of the

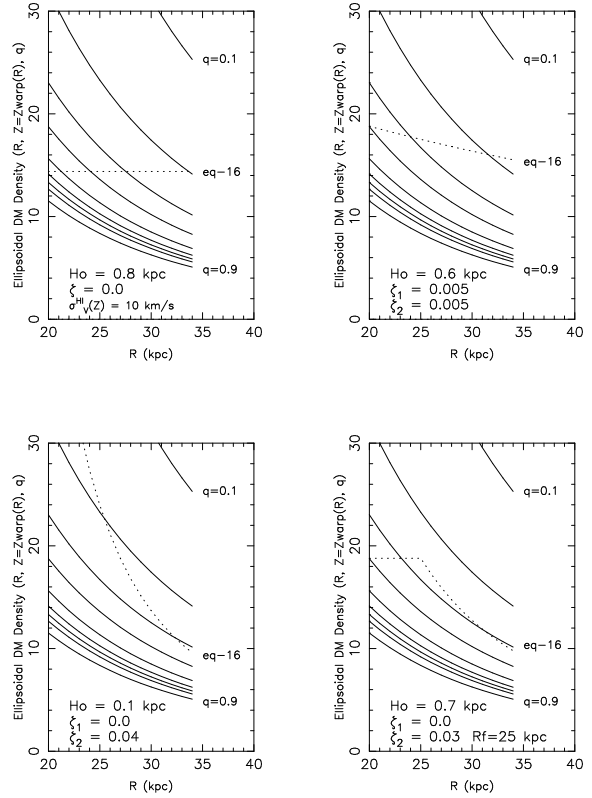


Fig. 13. We presents here plots of the right term of the equation 16 for different HI parameters (dotted curves). The full lines are the left term of eq. 16, DMH densities ρ_{DMH} , corresponding to values of q from 0.1 to 0.9. We see that the HI term has very different behaviours when we vary the H_0 and ζ parameters, so that the equation can determine "q" unambiguously. Densities are in units of $0.0002 M_\odot/\text{pc}^3$.

flatness of the rotation curve yields the condition:

$$\frac{\partial^2 \Phi_{galaxy}}{\partial R^2} + \frac{1}{R} \frac{\partial \Phi_{galaxy}}{\partial R} = 0 \quad (11)$$

We insert (11) in the Poisson equation written in cylindrical coordinates, which simplifies into (assuming the axisymmetry of the total galaxy potential):

$$4\pi G \rho_{galaxy} = \frac{\partial^2 \Phi_{galaxy}}{\partial Z^2} \quad (12)$$

We show in Fig 12 the different densities in the outer parts, in order to simplify the term

$$\rho_{galaxy} = \rho_\star + \rho_{bulge} + \rho_{HI} + \rho_{DMH}$$

We see that the bulge density is clearly negligible, while after $R \geq 20 \text{ kpc}$, the dark matter dominates largely the HI term. We note that the dark matter density considered for the graphic corresponds to $q = 0.5$; it is comparable

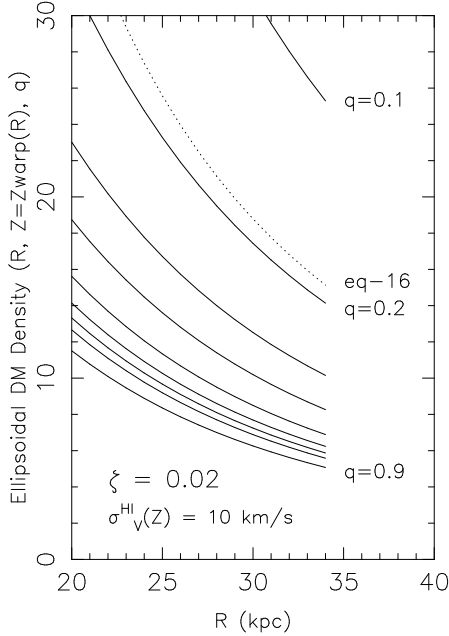


Fig. 14. We search here the solution of the equation (16) for the flaring value of NGC 891: $\zeta_1 = \zeta_2 = \zeta = 0.02$. We took here σ_{HI} isotropic. The value $q = 0.2$ is a good solution in average, the curve being nicely "parallel" to the DMH density curves. Densities are in units of $0.0002 M_{\odot}/pc^3$.

for $q = 0.8$, but twice higher for $q = 0.2$, so that the domination of the dark matter in the outer parts is quite certain. We may thus write

$$\rho_{galaxy}(R \geq 20 \text{ kpc}) \approx \rho_{DMH} \quad (13)$$

Combining finally the vertical Jeans equation (10), the Poisson equation (12) and the density approximation (13) provides:

$$\rho_{DMH} = \frac{-\sigma_Z^2}{4\pi G} \frac{\partial^2 \ln \rho_{HI}}{\partial Z^2} + \left[\frac{-1}{4\pi G} \left(\frac{\sigma_R^2 - \sigma_Z^2}{R} \right) \left(Z \frac{\partial^2 \ln \rho_{HI}}{\partial R \partial Z} + \frac{\partial \ln \rho_{HI}}{\partial R} \right) \right] \quad (14)$$

The term " $\ln \rho_{HI}(R, Z)$ " is known since its radial distribution has been derived in section 2.1 and its vertical distribution $Z_0(R)$ has been modelled in previous sections:

$$\rho_{HI}(R, \Theta, Z) \approx \rho_{0,HI} \exp\left(-\frac{(R - R_g)^2}{2\sigma_g^2}\right) \exp\left(-\frac{(Z - Z_{warp}(R, \Theta))^2}{2Z_0^2(R)}\right) \quad (15)$$

The domain of validity of the equation (14) covers $R \sim 20-30$ kpc, where the dark matter density dominates. The

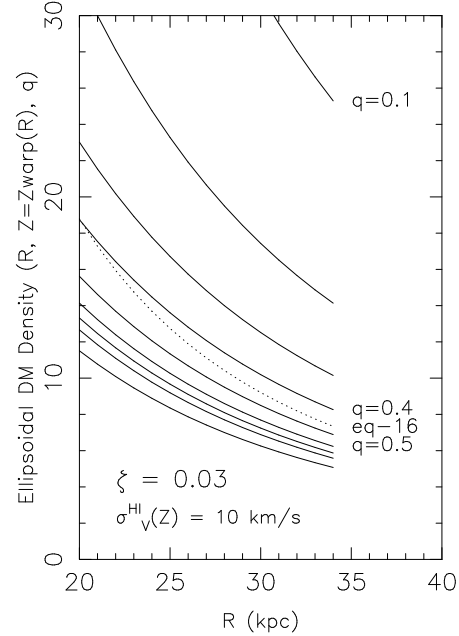


Fig. 15. Solution of the equation (16) for a greater value the flaring $\zeta = 0.03$, which could have been found without subtracting the warp. We observe that this value modifies substantially the flattening of the dark matter halo, pointing to an average value of $q \approx 0.4-0.5$. The method is thus very sensitive and the allowed range for ζ is between 0.015 and 0.035. Densities are in units of $0.0002 M_{\odot}/pc^3$.

term in brackets in the right hand side of (14), coming from the tilt of the velocity dispersion tensor, showed during computation to be totally negligible (as expected from the observations, see Malhotra 1995). For $\sigma_R - \sigma_Z = 5$ km/s, this term represents no more than 1 % of the first term. So that inserting (15) in the simplified (14) provides finally:

$$\rho_{DMH}(\rho_{0,DMH}(q), R \geq 20 \text{ kpc}) = \frac{\sigma_Z^2}{4\pi G Z_0^2(R)} \quad (16)$$

We notice that the dark matter density term does not here depend on Z , since the information on the flattening "q" is in fact included in the central density $\rho_{0,DMH}(q)$, derived from the rotation curve fit. In the equation (16), the vertical velocity dispersion of the gas, σ_Z , carries much of the uncertainty. This quantity is frequently approached, in the literature, through $\sigma_Z \approx \sigma_R$, but this is doubtful. The interstellar gas is under the form of small dense clumps, and the vertical component of its velocity dispersion should be smaller than the radial component, in the same qualitative manner as the stars.

We draw in Fig 13 the behaviour of equation (16) in its

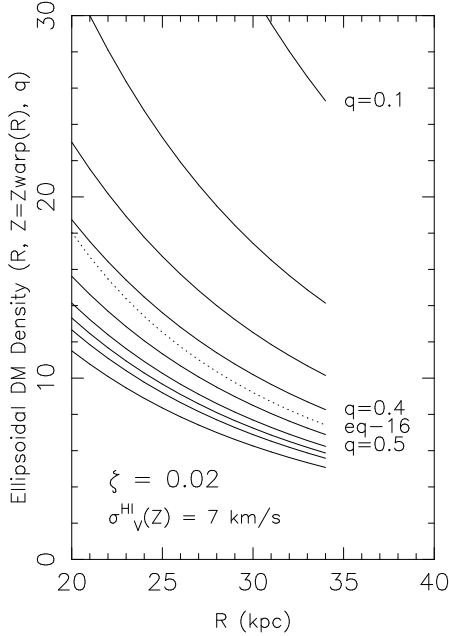


Fig. 16. Solution of the equation (16) for an anisotropic model of the HI velocity dispersion: $\sigma_{HI,Z} = 7$ km/s and $\sigma_{HI,R} = 10$ km/s. We observe that it rounds substantially the DMH, pointing to an average flattening of $q \approx 0.4 - 0.5$. Densities are in units of $0.0002 M_{\odot}/pc^3$.

domain of validity, intending to show its usefulness to derive q . The figure Fig 14 is the effective solution for our problem (i.e. the value of $\zeta = 0.02$ found in the previous spectral cube modeling section). We see that for a vertical velocity dispersion equal to the velocity dispersion in the plane, the average value of the flattening is $q \approx 0.2$, pointing to a very flattened DMH. We draw in Fig 15 the effects of changing the flaring up to a value of $\zeta = 0.03$: this rounds the DMH, with $q = 0.4 - 0.5$. We draw in Fig 16 the effects of changing the vertical velocity dispersion of the gas to a lower value of $\sigma_{HI,Z} = 0.7 \sigma_{HI,R}$. This makes also the DMH rounder at $q = 0.4 - 0.5$.

The method shows up to be conclusive, reflecting small variations of the ζ -flaring coefficient and the vertical velocity dispersion. We also note that there should exist a lower limit for the HI vertical velocity dispersion ($q \leq 1.0$): we find for NGC 891 that $\sigma_{HI,Z} \geq 5.5$ km/s. A summary of the values of q as a function of flaring parameter and HI z -velocity dispersion is listed in Table 2.

6. Conclusion

It was unfortunate that NGC 891 was found to have a warp which is maximum just along the line of sight, so

Table 2. Flattening of the DMH of NGC 891 ($R_c = 14$ kpc)

flaring ζ	vertical dispersion $\sigma_{HI,Z}$ (km/s)	flattening q
0.02	10	0.2
0.03	10	0.4-0.5
0.02	7	0.4-0.5

that the modeling of its HI flaring could not be as accurate as we could hope. Despite this difficulty, we have shown that it is possible to determine the HI plane thickness and the flaring for this quasi edge-on spiral galaxy using sequences of synthetic data cubes. The warp of high amplitude for NGC 891 is also a nice explanation for the observed strong variation with Z of the rotational velocities, a behaviour detected previously by several authors. We finally stress that the method seems efficient enough to constrain the DMH flattening of every inclined galaxy for which we can determine the following quantities:

$\sigma_{HI,Z}$ [from a moment 2 map or face-on galaxies]

$R_c, \rho_{0,DMH}(q)$ [from fits of the rotation curve]

H_0, ζ [from a 3D spectral cube modeling]

Noteworthy, the halo flattening found in this work is similar to the result of R. Olling on NGC 4244, both suggesting very flattened halos. It thus may become now interesting to test the dark matter model predicted by Pfenniger & Combes, a warped disk of H_2 cold molecular gas. We shall present in a forthcoming paper the results of our method applied to other galaxies with interferometric HI data cubes.

Acknowledgements. J.-F. Becquaert is grateful to Rob Olling, Konrad Kuijken, Frederic Masset, Linda Sparke and Roelof Bottema for useful and miscellaneous discussions about warps and halos. We specially thank Daniel Pfenniger for his nice comments and M. Rupen for the use of his data of NGC 891 in digital form.

References

- Binney, J.: 1992, ARAA 30, 51
- Binney, J. & Tremaine, S. 1987, "Galactics Dynamics", Princeton University Press, Princeton, New Jersey. [BT87]
- Bottema, R., van der Kruit, P.C., & Valentijn, E.A. 1991, A&A 247, 357-367
- Briggs, F. H. 1990, ApJ 352, 15
- Casertano, S. 1983, MNRAS 203, 735
- Combes, F. & Arnaboldi, M. 1996, A&A
- Corradi, R. L. M. & Capaccioli, M. 1990, A&A 237, 36
- de Zeeuw P.T., Pfenniger D.: 1988, MNRAS 235, 949
- David L.P., Jones C., Forman W.: 1995, ApJ, 445, 578
- Dame T.M., Ungerechts H., Cohen R.S. et al: 1987, ApJ 322, 706
- Dickey J.M., Hanson M.M., Helou G., 1990, ApJ 352, 522
- Dubinski, J. 1994, ApJ 431, 617
- Dubinski, J. & Carlberg, R.G. 1991, ApJ 378, 496

Freeman K.C.: 1993, in "Physics of Nearby Galaxies: Nature or Nurture?", ed. T.X. Thuan, C. Balkowski & J.T. Thanh Van, Editions Frontières, p. 201
 Lake, G. & Feinswog, L. 1989, AJ 98, 166
 Malhotra, S. 1995, ApJ 448, 138
 Masset, F. & Tagger, M. 1997, A&A, 318, 747
 Merrifield, M.R. 1992, AJ 103,1552
 Olling, R. P. 1995 Thesis Work, Columbia University
 Olling, R. P. 1995, AJ 110, 591
 Olling, R. P. 1996, AJ 112, 457
 Pfenniger, D. Combes, F., Martinet, L. 1994, A&A 285, 79
 Pfenniger, D. & Combes, F. 1994, A&A 285, 94
 Rupen, M.P. 1991a, AJ 102, 48
 Rupen, M.P. 1991b, Thesis Work, Princeton University
 Sackett P.D., Rix H-W., Jarvis B.J., Freeman K.: 1994, ApJ 436, 629
 Sackett, P.D. & Sparke, L.S. 1990, ApJ 361, 408
 Sackett, P.D. & Pogge, R.W. 1995, in "Dark Matter" Maryland Conference, October 1994, American Institute of Physics Press, p.
 Sancisi R., Allen R.J.:1979, A&A 74, 73
 Sparke, L.S. & Casertano, S. 1988. MNRAS 234, 87
 Steiman-Cameron T.Y., Kormendy J., Durisen R.H.: 1992, AJ 104, 1339
 Swaters R.A., Sancisi R., van der Hulst J.M.:1997 A&A, preprint
 Tubbs A.D., Sanders R.H.: 1979, ApJ 230, 736
 Van der Kruit, P.C. 1981, A & A 99, 298
 Zaritsky, D. & White, S.D.M. 1994, ApJ 435, 599

7. Appendix A: Non-cylindrical motions in galaxies

Let us consider a very flattened Kuzmin potential to represent the whole galaxy,

$$\Phi(R, Z) = \frac{GM}{\sqrt{R^2 + (a_0 + |Z|)^2}}$$

We expand $v_c^2 = R \frac{\partial \Phi}{\partial R}$ assuming $a_0 \ll Z \ll R$, obtaining:

$$v_c(z) = v_0 \left(1 - \frac{3}{4} \left(\frac{Z}{R}\right)^2\right)$$

Applying this formula for NGC 891, at $R = 10$ kpc and $Z = 3$ kpc gives for $v_0 = 225$ km/s a loss of velocity of about 15 km/s. A vertical gradient of velocity is thus generally expected in galaxies. We include explicitly this gradient in the model in multiplying the disk velocity by a factor $f_V(Z)$, which is chosen in practice to be $(1 - \frac{3}{4}(\frac{Z}{R})^2)$.

8. Appendix B: Derivation of the spiral arm velocities

We entered in the modeling of the spiral arms their perturbed velocities associated with the mode m (practically, $m = 2$). Using Euler's equation, BT87 estimated that V_R and V_Θ are of the same order and thus the continuity equation could be simplified, (pages 356-359) resulting in the

formula of the perturbed radial velocity associated with the mode m : (under adaptations for the present context)

$$V_R(m) = -\frac{m\Omega - \omega}{k_m} \frac{A_m}{A_0} \left[\frac{1}{R} \cos(k_m R + m(\Theta - \Theta_m))\right]$$

The perturbed tangential velocity associated with the mode m is obtained from formula (6-36) of BT87, yielding:

$$V_\Theta(m) = \frac{-2B}{k_m} \frac{A_m}{A_0} \left[\frac{1}{R} \sin(k_m R + m(\Theta - \Theta_m))\right]$$

"B" being Oort's second "constant". It is noteworthy that V_R changes sign at corotation, while V_Θ does not. The kinematical parameters a-priori unknown in the formula above are derivable from a multi-component fit of the rotation curve (Fig 4): the value of $\Omega = \frac{V_{rot}}{R}$, $\kappa = \sqrt{R \frac{d\Omega^2}{dR} + 4\Omega^2}$ and $B = B(R) = -\frac{\kappa^2}{4\Omega}$. The main modification in the spectral cube construction due to the consideration of these perturbed velocities, is to change the formula of the line-of-sight velocity, which is now:

$$V_{los}(m = 0) = V_{sys} + V_{rot} \sin I \cos \Theta f_V(Z)$$

$$V_{los}(m \neq 0) = V_{sys} + [(V_{rot} + V_\Theta(m)) \sin I \cos \Theta + V_R(m) \sin I \sin \Theta] f_V(Z)$$

9. Appendix C: potentials for generalized dark matter densities

Simulations of spherical infall in an Einstein-de Sitter universe onto seeds perturbations and onto density peaks in power cosmologies result in objects with $\rho \propto R^{-\alpha}$, $1.6 \leq \alpha \leq 2.25$ (Dubinski & Carlberg, 1991). This is close enough to the isothermal profile (i.e. R^{-2}), which is often adopted for the sake of simplicity. However, Lake & Feinswog (1989) showed that profiles in R^{-3} and even R^{-4} were also possible to obtain a good fit of observed rotation curves. Taking this result into account, we consider hereafter the generalized family of densities:

$$\rho_p(q) = \frac{\rho_{0,DMH}}{\left(1 + \frac{R^2}{R_c^2} + \frac{Z^2}{R_c^2 q^2}\right)^p} \quad (p \geq 0)$$

This density model recovers, for $p = 1$, the formula of the isothermal density profile used in this article and previously by other authors. We give here the formula of the dark matter potential for $p \neq 1$, which can be derived using formula 2.6 of de Zeeuw & Pfenniger (1988), and the new variable $(x = \frac{R_c}{\sqrt{a+q^2 R_c^2}})$, providing:

$$\Phi_{DMH}(R, Z) = -\frac{2\pi}{1-p} G \rho_{0,DMH} q R_c^2 \int_0^{\frac{1}{q}} \frac{[1 + \frac{x^2}{R_c^2} (\frac{R^2}{\epsilon^2 x^2 + 1} + Z^2)]^{1-p}}{\epsilon^2 x^2 + 1} dx$$

The rotation curve contribution is, from that moment, straightforward.

This article was processed by the author using Springer-Verlag L^AT_EX A&A style file L-AA version 3.